

# Multilaminar networks of cortical neurons integrate common inputs from sensory thalamus

Nicolás A Morgenstern, Jacques Bourg & Leopoldo Petreanu

Neurons in the thalamorecipient layers of sensory cortices integrate thalamic and recurrent cortical input. Cortical neurons form fine-scale, functionally cotuned networks, but whether interconnected cortical neurons within a column process common thalamocortical inputs is unknown. We tested how local and thalamocortical connectivity relate to each other by analyzing cofluctuations of evoked responses in cortical neurons after photostimulation of thalamocortical axons. We found that connected pairs of pyramidal neurons in layer (L) 4 of mouse visual cortex share more inputs from the dorsal lateral geniculate nucleus than nonconnected pairs. Vertically aligned connected pairs of L4 and L2 and 3 (L2/3) neurons were also preferentially contacted by the same thalamocortical axons. Our results provide a circuit mechanism for the observed amplification of sensory responses by L4 circuits. They also show that sensory information is concurrently processed in L4 and L2/3 by columnar networks of interconnected neurons contacted by the same thalamocortical axons.

The integration of sensory information arriving from the thalamus to primary sensory cortices has been one of the most studied cortical computations<sup>1,2</sup>. In the primary visual cortex (V1), ascending thalamocortical (TC) inputs from the dorsal lateral geniculate nucleus (dLGN) preferentially innervate neurons in L4 and send sparser projections to L2/3 and L5 neurons<sup>3–5</sup>. Novel sensory representations emerge in the cortex after cortical neurons integrate convergent thalamic input<sup>6</sup>.

The relative contributions of TC input and local cortical circuits in shaping the functional properties of V1 neurons have been extensively investigated in L4. Results from previous studies are consistent with Hubel and Wiesel's classic feedforward model<sup>7</sup>, which proposes that the convergence of specific spatially arranged dLGN inputs onto L4 neuron results in the emergence of orientation tuning independently of the local cortical circuitry. Cooling or optogenetically mediated cortical silencing experiments demonstrate that intracortical connections amplify L4 responses with no changes in their tuning properties<sup>8–12</sup>. Modeling studies suggest that recurrent local excitation could result in the observed amplification of L4 signals<sup>13–15</sup>. An untested prediction from these models is that L4 neurons receiving common thalamic input should be preferentially interconnected so that specific signals become amplified without changes in tuning properties. Pyramidal neocortical neurons assemble in interdigitated, highly interconnected subnetworks<sup>16,17</sup>. In L2/3, subnetworks of connected pyramidal neurons share common local L4 inputs<sup>18</sup>. However, how local connectivity relates to long-range connectivity in sensory cortex remains unexplored. It is unknown whether, as predicted by the models of amplification by local recurrent networks, cortical neurons receiving common long-range thalamic inputs are preferentially connected to each other. Also, taking into account that dLGN axons innervate neurons in many cortical layers<sup>6,19–21</sup>, it is also unknown whether multilaminar assemblies of connected neurons integrate

common dLGN inputs or if instead TC information is differentially routed to neurons in different layers.

We measured how connected cells in L4 and L2/3 integrate dLGN input in mouse V1. Using Channelrhodopsin-2 (ChR2)-assisted circuit mapping<sup>22,23</sup> (CRACM), we measured the strength and the dendritic distribution of dLGN inputs to pyramidal neurons. We found that in addition to the strong innervation of L4 neurons, dLGN inputs strongly innervate neurons in lower L2/3. By combining optical high-throughput minimal stimulation of ChR2-expressing (ChR2<sup>+</sup>) axons with simultaneous multiple whole-cell recordings, we developed a technique to measure how local and long-range connectivity relate to each other. We found that connected neurons in L4 share more common thalamic input than nonconnected pairs. Moreover, L4→L2/3 connected pairs received more common dLGN input than unconnected pairs, indicating that TC axons specifically connect with multilaminar networks of connected neurons in L4 and L2/3. These connectivity patterns are consistent with the models of L4 cortical amplification by recurrent connections. Furthermore, our results indicate that, rather than flowing serially from L4 to L2/3, thalamic afferents are simultaneously processed by interconnected fine-scale neuronal assemblies encompassing both layers organized around common TC axons.

## RESULTS

### dLGN→V1 inputs innervate L4 and L2/3 pyramidal neurons

We injected adeno-associated virus (AAV) encoding ChR2-Venus into dLGN to label TC projections to V1. dLGN axons were found in all cortical layers. The densest projection was in L4, followed by L2/3, where Venus-expressing axons could be seen projecting up to L1, their density becoming progressively lower closer to the pia (Fig. 1a). dLGN also sent sparser projections to L5 and L6. We quantified the strength of the TC projection to different populations of V1 pyramidal

Champalimaud Neuroscience Programme, Champalimaud Center for the Unknown, Lisbon, Portugal. Correspondence should be addressed to L.P. (leopoldo.petreanu@neuro.fchampalimaud.org).

Received 24 March; accepted 26 May; published online 4 July 2016; doi:10.1038/nn.4339

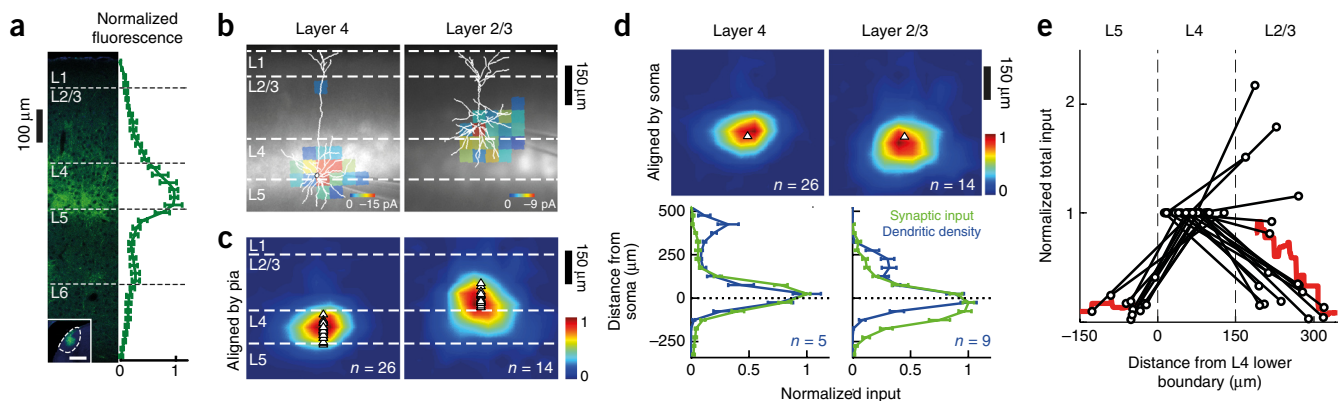


**Figure 1** dLGN→V1 inputs strongly innervate L4 and deep L2/3 pyramidal neurons. **(a)** Confocal image of Venus-labeled (green) dLGN axons in V1 and normalized vertical profile of the axonal fluorescence distribution, mean of 3 mice  $\pm$  s.e.m. Blue: DAPI staining. Inset: injection site in dLGN (scale bar: 500  $\mu$ m). **(b)** Examples of sCRACM maps overlaid on reconstructions of the dendritic arbor and on fluorescence images showing dLGN axons expressing Chr2. **(c)** Average sCRACM maps aligned by pia position (white triangles, soma position). **(d)** Top: average sCRACM maps aligned by soma (white triangles). Bottom: vertical profile of the distribution of synaptic input (green) and the dendritic length density aligned by soma (blue), given as mean  $\pm$  s.e.m. **(e)** Total dLGN input (sum of all pixels in the sCRACM maps) to vertically aligned pairs of neurons (17 L4–L2/3 pairs, 11 L4–L5 pairs; from 18 mice). Input is normalized to L4 values. Thick red line, moving average (75- $\mu$ m window) for L2/3 and L5 values.

neurons in acute brain slices by photostimulating Chr2<sup>+</sup> synapses in the presence of tetrodotoxin (TTX) and 4-aminopyridine (4-AP) while performing whole-cell recordings from pyramidal neurons using subcellular CRACM (sCRACM). sCRACM allows rapid mapping of the distribution of monosynaptic inputs from Chr2<sup>+</sup> axons onto the dendrites of the recorded neurons<sup>23</sup> (Fig. 1b–d). To account for the variability in expression levels across slices, we sequentially recorded vertically aligned pairs of neurons under identical laser powers. We assessed the relative strength of dLGN inputs by

adding sCRACM responses over the entire dendritic trees of L2/3 or L5 neurons and comparing them to the values obtained from an L4 pyramidal neuron recorded in the same slice (Fig. 1e). The strengths of dLGN→L2/3 inputs depended on the cortical depth of the postsynaptic neurons. Inputs to neurons within 100  $\mu$ m of L4 were on average 85% as strong as those to L4, while inputs to more superficial neurons were much weaker. dLGN inputs onto L4 pyramidal neurons were located mainly on dendrites surrounding their somata and also on their apical dendrites (Fig. 1b–d). L2/3 pyramidal neurons received

**Figure 2** Method for assessing how local and long-range connectivity relate to each other. **(a)** Local connectivity test. Presynaptic spiking elicited for each neuron (top) and the traces simultaneously recorded in the other neuron (bottom). Traces are the mean of 100 repetitions. **(b)** Image of a brain slice (same experiment as in a) showing the recording pipettes and the photostimulation grid. 1 and 2 indicate the neurons shown in a; lettered arrows indicate locations shown in e–g. **(c)** Maps of mean eEPSC charge (top) and response probability (bottom) across photostimulated locations in b for each neuron in the pair. White triangles, soma positions. **(d)** Top, map of mean eEPSC charge for the pair for all photostimulated locations (average of top panels in c). Mean number of inputs is calculated as (mean eEPSC for the pair)/(TC unitary input size). White circles indicate locations with correlated eEPSCs. Bottom, fraction of correlated locations as function of the mean number of inputs. Bin size, 1 input. Shaded area, range used for analyses in Figures 4 and 5. Pixels with values within that range are marked with black dots in top panel. **(e–g)** Example plots (top) and traces (bottom) for correlated (e,g) and uncorrelated (f) responses from locations where a putative single axon (e,f) or more than one axon (g) was photostimulated. Temporal sequence of traces is from left to right and from top to bottom. Inset, superimposed traces recorded on one of the recorded neurons. Traces correspond to the locations indicated in b (arrowheads). An unrecorded neuron is represented in gray in f. Laser pulses were delivered at the beginning of each trace.

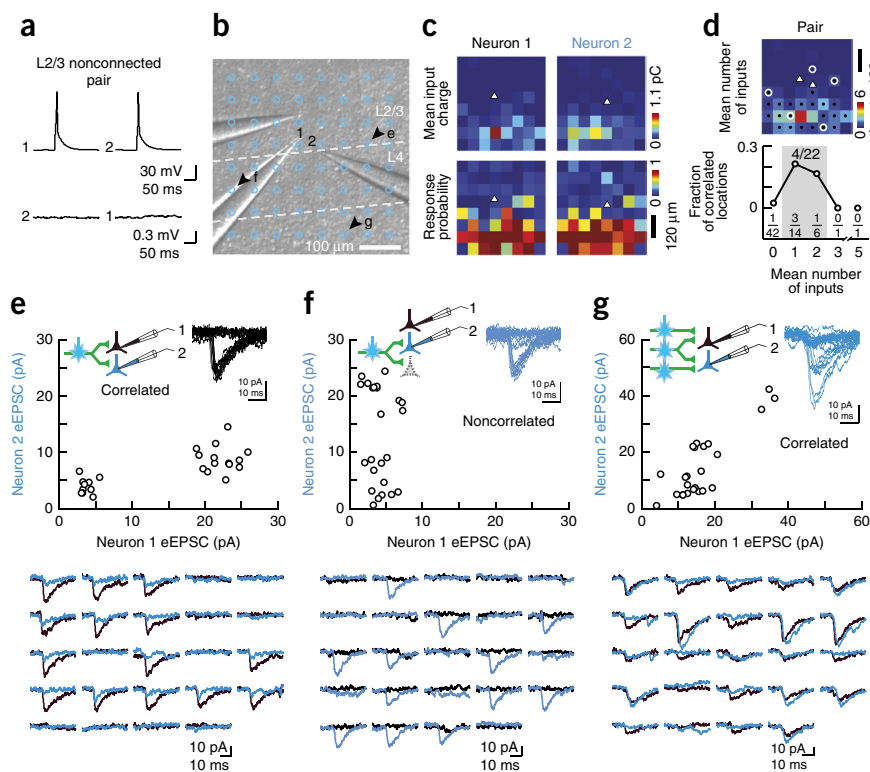
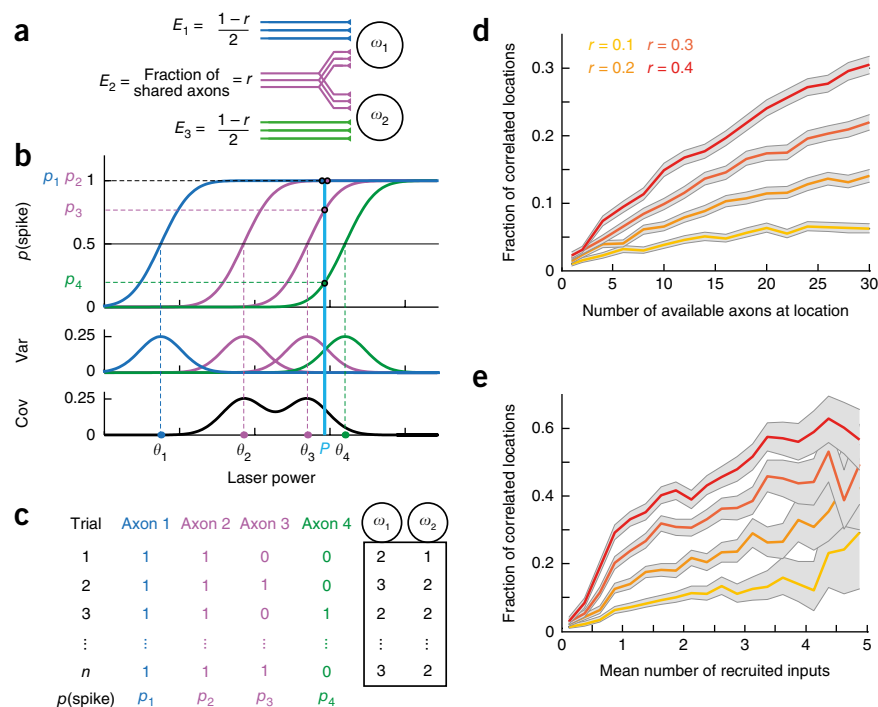


**Figure 3** Simulations of how cofluctuations depend on the number of recruited inputs and the fraction of shared axons. **(a)** Three different populations of axons with different connectivities project to a pair of neurons with membrane potentials  $\omega_1$  and  $\omega_2$  expressed in number of unitary inputs. **(b)** Top: spiking probability ( $p$ ) for an example location with 4 axons as function of laser power. Each axon  $i$  has its own threshold  $\theta_i$ . Colors, connectivity groups from **a**. Middle: variance (var) of the spiking. Bottom: covariance (cov) of  $\omega_1$  and  $\omega_2$ . When photostimulating with a given laser power ( $P$ ), only shared axons that spike with probability  $0 < p_i < 1$  contribute to the covariance (axon 3 in this example). **(c)** We simulated sampling from a random population of axons with different thresholds and connectivity with laser power  $P$ . At each trial, axons spiked with probability  $p_i$ . 1, spike; 0, no spike. An added noise factor in the responses was omitted for clarity (see Online Methods). **(d)** Fraction of correlated inputs as a function of the number of axons available for photostimulation when using a single laser power. Colors correspond to different fractions of shared input ( $r$ ). **(e)** Fraction of correlated inputs as a function of the number of inputs recruited at each location using a single laser power. The same number of axons was available across locations. The number of inputs is obtained by averaging the responses from both neurons. Shading, 95% confidence interval.



dLGN inputs mainly in their lower basal dendrites. dLGN inputs to L5 pyramids were weaker than those to L4 or L2/3. When detected in L5 pyramids, dLGN inputs targeted the perisomatic dendrites and apical dendritic segments in L4 (**Supplementary Fig. 1**). On average dLGN→L5 inputs were only 16% as strong as those contacting L4 pyramids. Thus, in addition to strongly innervating L4, dLGN inputs mainly target neurons in lower L2/3.

### Measuring local and long-range TC connectivity

We then measured how interconnected subnetworks of excitatory neurons in L4 and L2/3 integrate dLGN input. Excitatory L4 and L2/3 neurons in V1 were identified by their laminar position and their intrinsic firing patterns (**Supplementary Fig. 2**). Local connectivity was assessed by evoking action potentials in one of the recorded neurons while simultaneously monitoring membrane potential changes in all the other patched neurons (**Fig. 2a**). We measured shared long-range TC connectivity in simultaneously recorded neurons by photostimulating ChR2<sup>+</sup> dLGN axons in the vicinity of the recorded neurons using a laser beam (**Fig. 2** and **Supplementary Fig. 3**). ChR2<sup>+</sup> axons can be photostimulated in brain slices even when severed from their parent somata<sup>22</sup>. Individual ChR2<sup>+</sup> axons have different light intensity thresholds to spike, and spiking probability increases as a function of laser power<sup>22</sup>. At intermediate illumination intensities, spikes can be elicited in a regime of successes and failures, akin to minimal stimulation using electrodes<sup>22,24</sup>. Using galvanometer mirrors, we repeatedly photostimulated dLGN axons in a grid pattern over V1 slices while simultaneously recording from multiple L4 and L2/3 pyramidal neurons (**Fig. 2b**). Photostimulation of dLGN axons was done at low laser intensities in order to maximize the excitation of axons in a regime of failures and successes (**Fig. 2c**). Additionally, these photostimulation conditions resulted in subthreshold depolarizations

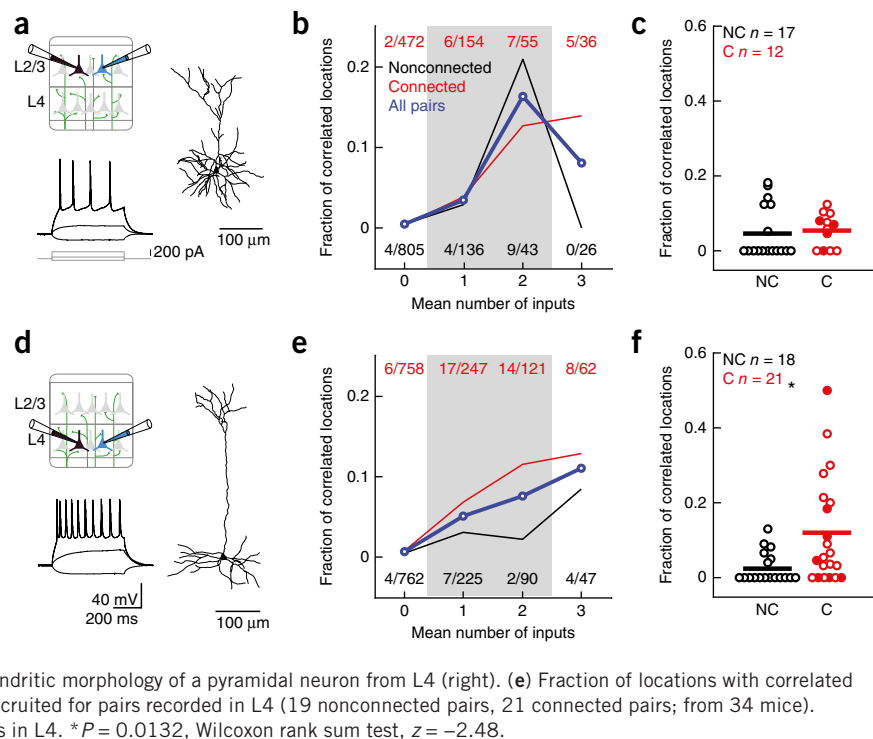
of L4 and L2/3 neurons, ensuring that evoked excitatory post-synaptic currents (eEPSCs) recorded in L4 and L2/3 originated from direct monosynaptic dLGN inputs and not from polysynaptic excitation involving other cortical neurons (**Supplementary Fig. 4** and Online Methods). If a minimally stimulated ChR2<sup>+</sup> axon connects to a pair of simultaneously recorded neurons, their optically evoked eEPSCs cofluctuates across stimulations<sup>25–28</sup> (**Fig. 2e**). Conversely, if a minimally stimulated axon innervates only one of the recorded neurons, the amplitude of its eEPSCs varies independently (**Fig. 2f**). In locations where more than one connecting axon is stimulated, eEPSCs also cofluctuate when one of the axons is driven unreliably and connects with the recorded pair (**Fig. 2g**). Thus, correlations measured from locations where one or several axons are stimulated reveal shared inputs.

Given the uneven density of ChR2<sup>+</sup> axons in the slice, photostimulation excited varying numbers of axons across locations, eliciting eEPSCs with different mean charges (**Fig. 2c**). We estimated the unitary dLGN input strength from locations that resulted in apparent minimal stimulation of isolated single dLGN axons and showed failures and successes of the recorded eEPSCs (**Fig. 2c,e,f**). eEPSCs from putative single dLGN axons were slightly larger in L2/3 than in L4 neurons (mean L4 eEPSC charge  $0.13 \pm 0.07$  pC, range 0.01 – 0.87 pC,  $n = 880$  connections from 52 mice; mean L2/3 eEPSC charge  $0.16 \pm 0.10$  pC, range 0.02 – 0.95 pC,  $n = 628$  connections from 44 mice; Wilcoxon rank sum test,  $z = 7.64$ ,  $P = 2.2 \times 10^{-14}$ ).

For each location on the grid, we approximated the average number of inputs contacting the pair as the mean eEPSCs from both neurons divided by the unitary dLGN input size (**Fig. 2d**). This metric is a measure of the mean number of connecting photostimulated axons, but with shared axons counted twice. Correlated responses were elicited in a fraction of the photostimulated locations and from sites recruiting different numbers of inputs (**Fig. 2d**).

**Figure 4** Interconnected neurons in L4 receive common dLGN inputs. (a) Scheme of paired recordings from L2/3 neurons (top left). Typical firing pattern of a L2/3 pyramidal neuron (bottom left). Gray traces, current injection steps. Example dendritic morphology of a pyramidal neuron from L2/3 (right). (b) Fraction of locations with correlated inputs as a function of the mean number of inputs recruited for pairs recorded in L2/3 (17 nonconnected pairs, 12 connected pairs; from 26 mice). Bin size, 1 input. The first 4 bins are plotted, as they contained most of the data. See **Supplementary Figure 5** for all data. Exact fractions of correlated locations in each bin are shown for connected and nonconnected pairs. (c) Fraction of correlated locations for individual pairs in L2/3. Each dot corresponds to a single pair. Horizontal lines, mean. Only locations within the same range of mean number of inputs were compared across pairs (shaded area in **b**). NC, nonconnected pairs; C, connected pairs. Filled dots, bidirectionally connected pairs.  $P = 0.4595$ , Wilcoxon rank sum test,  $z = -0.74$ .

(d) Scheme of paired recordings from L4 neurons (top left). Typical firing pattern of an L4 pyramidal neuron (bottom left). Example dendritic morphology of a pyramidal neuron from L4 (right). (e) Fraction of locations with correlated inputs as a function of the mean number of inputs recruited for pairs recorded in L4 (19 nonconnected pairs, 21 connected pairs; from 34 mice). (f) Fraction of correlated locations for individual pairs in L4.  $*P = 0.0132$ , Wilcoxon rank sum test,  $z = -2.48$ .



### Correlations depend on the number of stimulated axons and the fraction shared

As photostimulation can reveal shared inputs even from locations where several axons are driven, we modeled how eEPSC correlations in pairs of simultaneously recorded neurons are expected to depend on the number of axons stimulated and the fraction of shared input. We simulated sampling randomly from a population of axons with different connectivity and thresholds (**Fig. 3a,b**) with a fixed laser power. This is analogous to photostimulating presynaptic ChR2<sup>+</sup> axons in different locations, as in our experiments. As unreliable photostimulation of axons only occurs within a narrow light intensity range<sup>22</sup>, at any given laser power only minimally stimulated shared axons contribute to the covariance of simultaneously recorded eEPSCs (**Fig. 3b,c**). As a consequence, the probability of finding correlated eEPSCs increased with the number of axons available at each photostimulation site (**Fig. 3d**). Similarly, when simulating photostimulation at sites with the same number of available axons, the fraction correlated increased with the number of inputs recruited at each location (**Fig. 3e**). Thus, when comparing the fraction of shared axons between groups, measurements from locations with similar numbers of photostimulated axons must be used. For locations with equal number of photostimulated inputs, correlations were higher when a larger fraction of axons contacted both neurons (**Fig. 3e**), allowing comparisons of shared input between populations.

### Interconnected neurons in L4 receive common dLGN inputs

We next investigated whether dLGN inputs differentially contacted pyramidal neurons in L4 and L2/3 depending on their local intralaminar connectivity. Pyramidal neurons in L4 and L2/3 had characteristic dendritic morphologies, as well as significantly different intrinsic properties (**Fig. 4a,d** and **Supplementary Fig. 2**) and intralaminar connection probabilities (**Table 1**). Thus, pyramidal neurons in L2/3 and L4 assemble in interconnected networks within their layers with different local connectivity and electrophysiological properties.

We photostimulated dLGN axons while performing simultaneous whole-cell recordings in pairs of L4 or L2/3 pyramidal neurons (**Fig. 4a,d**). As predicted by our simulations, the fraction of locations eliciting correlated responses increased as a function of the number of inputs recruited (**Fig. 4b,e**; in L2/3:  $P = 0$ ,  $\chi^2 = 88.47$ ; in L4:  $P = 0$ ,  $\chi^2 = 81.44$ ; Cochran-Armitage test for trend; see also **Supplementary Fig. 5**).

To compare the fraction of shared inputs across individual pairs, we calculated the fraction of photostimulated locations that elicited correlated inputs within the same range of mean number of inputs (**Fig. 4c,f**). Locations eliciting correlated inputs were 4.7-fold more abundant in L4 connected pairs than in nonconnected ones (**Fig. 4f**), indicating that they shared a larger proportion of their TC inputs (**Fig. 3**). This difference was not observed in L2/3 (**Fig. 4b,c**). Unidirectionally and bidirectionally connected pairs shared a similar fraction of TC inputs (**Fig. 4c,f**). The strength of the local connections was a poor predictor

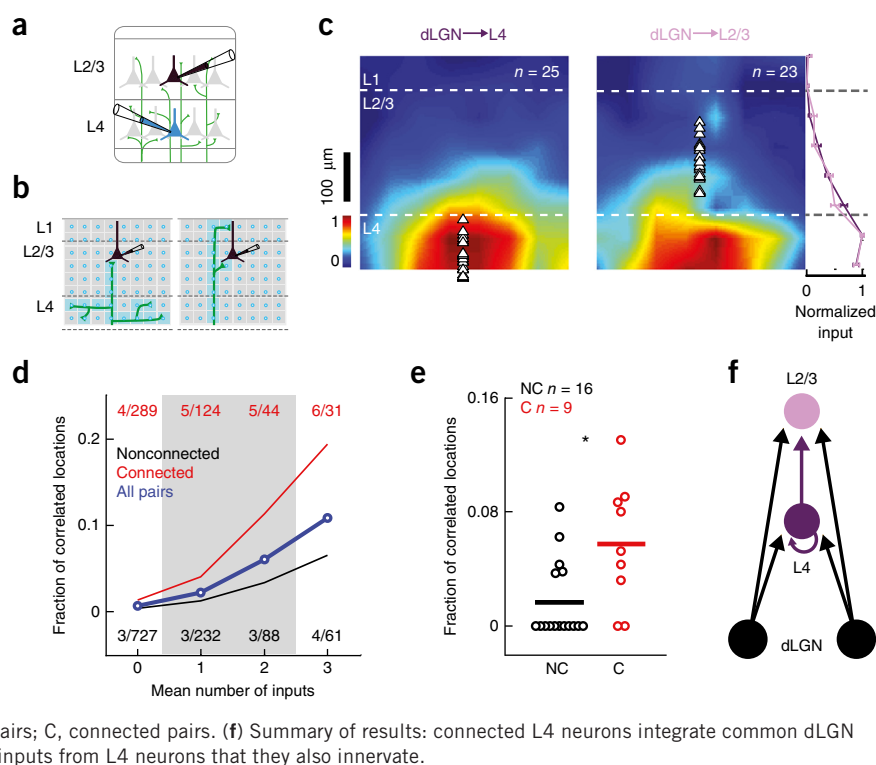
**Table 1** Connection probability and synaptic properties of L4 and L2/3 pyramidal neurons in V1

	Postsynaptic	Presynaptic	
		L4	L2/3
L2/3	CP (found/tested)	14.5% (16/110)	24.1% (14/58)
	Mean $\pm$ s.e.m.	0.21 $\pm$ 0.05 mV	0.45 $\pm$ 0.17 mV
	Median	0.14 mV	0.14 mV
	Range	0.10–0.49 mV	0.09–2.76 mV
	Coeff. of var. $\pm$ s.e.m.	0.89 $\pm$ 0.18	0.85 $\pm$ 0.16
L4	CP (found/tested)	47.6% (39/82)	0% (0/110)
	Mean $\pm$ s.e.m.	0.21 $\pm$ 0.03 mV	
	Median	0.15 mV	
	Range	0.07–0.55 mV	
	Coeff. of var. $\pm$ s.e.m.	1.08 $\pm$ 0.13	

Connection probability (CP): L4→L4 versus L2/3→L2/3 (data from 93 mice),  $P = 0.00496$ ,  $z = 2.81$ . L4→L4 versus L4→L2/3 (data from 117 mice),  $P = 0$ ,  $z = 5.01$ . L2/3→L2/3 versus L4→L2/3 (data from 86 mice),  $P = 0.1236$ ,  $z = 1.54$ . Coeff. of var., coefficient of variation.



**Figure 5** dLGN axons preferentially innervate L4→L2/3 connected pairs. **(a)** Scheme of paired recordings from vertically aligned L4 and L2/3 neurons. **(b)** Photostimulated locations eliciting eEPSCs (blue squares) track the trajectories and arborizations of the axons contacting the recorded neuron. Axons contacting L2/3 neurons preferentially arborizing in L4 (left) can be distinguished from those skipping L4 (right). **(c)** Average photostimulation maps aligned by pia for L4 and L2/3 recorded neurons (white triangles, soma positions). Right: normalized vertical profile of photostimulation maps, mean  $\pm$  s.e.m. **(d)** Fraction of locations with correlated inputs as a function of the mean number of inputs recruited for all the recorded vertical pairs (19 nonconnected pairs, 9 connected pairs; from 24 mice;  $P = 7.52 \times 10^{-13}$ ,  $\chi^2 = 51.4$ ; Cochran-Armitage test for trend). Bin size, 1 input. The first 4 bins are plotted, as they contained most of the data. See **Supplementary Figure 5** for all data. **(e)** Fraction of correlated locations for individual vertical pairs. \* $P = 0.0146$ , Wilcoxon rank sum test,  $z = -2.44$ . Horizontal lines, mean. Only locations within the same range of mean number of inputs were compared across pairs (shaded area in **d**). NC, nonconnected pairs; C, connected pairs. **(f)** Summary of results: connected L4 neurons integrate common dLGN inputs. dLGN axons contact L2/3 neurons receiving inputs from L4 neurons that they also innervate.



of the fraction of correlated locations (**Supplementary Fig. 6**). The increase in correlated inputs in connected L4 pairs could not be explained by differences in intersomatic distances between the groups of connected and nonconnected neurons (**Supplementary Fig. 7**). Thus, locally interconnected subnetworks in L4 receive more common dLGN input than nonconnected neighboring cells.

#### dLGN axons preferentially innervate L4→L2/3 connected pairs

Next we investigated whether a single population of dLGN axons contacted neurons in both L4 and L2/3 or, alternatively, whether laminar-specific populations of axons with different arborization patterns independently innervated the two layers. We simultaneously recorded from vertically aligned pairs of L4 and L2/3 pyramidal neurons (**Fig. 5a**) and photostimulated ChR2<sup>+</sup> dLGN axons in a grid pattern covering upper L4 and L2/3 as described above. When ChR2<sup>+</sup> axons are stimulated in a grid pattern while recording from a postsynaptic neuron, the locations that result in eEPSCs track the trajectories and arborizations of the axons contacting the recorded neurons<sup>22</sup> (**Fig. 5b**). The vast majority of the eEPSCs recorded in both L4 and L2/3 neurons were elicited when illuminating over L4. The laminar distribution of excited locations was indistinguishable between L4 and L2/3 recordings, indicating that dLGN axons connecting to L4 and L2/3 neurons have similar arborization patterns and overall trajectories (**Fig. 5c**). Thus, most of the axons contacting L2/3 neurons have few branches in L2/3 and heavily arborize in L4 (ref. 20), where they most likely also innervate L4 neurons.

We found L4→L2/3 connections in 14.5% of the recorded pairs, all unidirectional (**Table 1**), confirming that neurons in the recorded pairs belonged to different neuronal populations. We stimulated dLGN axons and analyzed eEPSCs covariance in simultaneously recorded pairs of L4 and L2/3 neurons. eEPSC were more highly correlated across trials in connected than in nonconnected pairs (**Fig. 5d,e**). Vertically connected pairs had on average 3.5-fold more correlated locations than nonconnected ones. Thus, L4→L2/3 connected

pairs are more likely to share dLGN input than nonconnected pairs. Hence, dLGN axons that skip the feedforward laminar hierarchy to contact L2/3 neurons preferentially connect with neurons receiving inputs from L4 neurons that they also innervate (**Fig. 5f**).

#### DISCUSSION

We investigated whether TC afferents preferentially connect with locally connected subnetworks of pyramidal neurons in mouse visual cortex. We found that dLGN projections to pyramidal neurons in the deep L2/3 were almost as strong as those terminating in the canonical TC recipient layer, L4. We also measured how local and TC connectivity relate to each other in granular and supragranular layers of V1. We found that dLGN axons preferentially targeted pairs of connected pyramidal neurons within L4. Moreover, L4→L2/3 connected pairs were also preferentially innervated by the same dLGN axons, demonstrating that common thalamic inputs are simultaneously integrated by vertically organized multilaminar networks of connected neurons.

#### Technical considerations

We developed a method to efficiently measure how local and long-range connectivity relate to each other. Common local cortical connectivity can be measured using multiple paired recordings<sup>29</sup>. Alternatively, shared inputs can be detected by measuring response correlations in postsynaptic neurons after laser-scanning photostimulation of the local circuitry by uncaging glutamate<sup>18,30</sup> or electrical minimal stimulation of afferent axons<sup>25–28</sup>. Our method relies on cofluctuation analysis of eEPSCs in simultaneous whole-cell recordings during optical stimulation of ChR2<sup>+</sup> axons. As ChR2<sup>+</sup> axons are excitable even when severed from their parent somata<sup>22</sup>, shared connectivity can be measured even when projections are not preserved in brain slices. Thus, our method can be applied to measure shared connectivity of afferent projections of any length scale. In addition, by using optical rather than electrical stimulation of axons, cofluctuations can be efficiently measured from many

stimulated locations, yielding measurements from a large number of axons per experiment.

We detected axons innervating pairs of recorded neurons by repeatedly stimulating them under illumination conditions that elicit unreliable axonal activation, resulting in eEPSC cofluctuations. In addition to failures of axonal photoactivation, failures of transmitter release can also contribute to fluctuations of eEPSCs amplitudes independently at each release site. Thus, synaptic failures lead to a decrease of eEPSC correlations in neurons receiving common input from the photostimulated axons. This would add noise to the cofluctuation analysis and mask measurements of shared connectivity. TC synapses are highly reliable<sup>31–33</sup>, and eEPSC decorrelations in connected pairs due to release failures are expected to be relatively low. When measuring common connectivity in neurons receiving inputs from less reliable synapses, we anticipated that more repetitions would be required to detect common input and compensate for the decorrelating effect of synaptic failures.

### Shared TC innervation of connected L4 neurons

We found that connected pyramidal L4 neurons shared more common dLGN inputs than nonconnected ones. As the convergence of specific spatially offset ON and OFF TC axons determines the tuning properties of the postsynaptic neurons<sup>8–10,12,34,35</sup>, L4 neurons sharing thalamic input are expected to have similar orientation and temporal phase preferences. Our results suggest that L4 neurons with similar functional properties will also be preferentially interconnected. This is consistent with recent experiments showing that cortical input to L4 neurons is tuned for the same orientation and temporal phase of the target neurons<sup>10</sup>. Therefore, experimental evidence strongly suggests that, as in L2/3 (refs. 36–38), excitatory neurons in L4 with similar tuning might also preferentially connect with each other. This connectivity pattern, in which locally interconnected neurons sample shared long-range inputs, also supports models of amplification without changes in tuning properties of TC responses by recurrent excitation<sup>13–15</sup>.

Unlike in L4 pairs, we did not detect a larger fraction of shared TC input in connected L2/3 neurons when compared to the unconnected ones. As TC axons selectively innervated L4→L2/3 connected pairs, connected L2/3 pairs could also share more TC inputs than nonconnected ones, given their tendency to receive common L4 inputs<sup>30</sup>. As we did not record from strongly connected L2/3 pairs (Supplementary Fig. 6), pairs in our data set would be predicted to have dissimilar receptive fields<sup>37</sup> and likely share relatively few bottom-up inputs. It remains to be determined whether strongly connected L2/3 neurons, given their similar and overlapping receptive fields, share common TC innervations like L4 neurons do.

### Integration of thalamic signals by multilaminar networks

We confirmed that the TC projection to mouse V1, like that in other sensory cortices, makes functional monosynaptic connections with neurons in L5 and lower L2/3 in addition to its main target population in L4 (refs. 21,23,39). Neurons in the deeper half of L2/3 received on average 85% as much input as L4 neurons. Thus, direct TC excitation, in addition to L4 inputs<sup>40–42</sup>, might exert significant influence on the tuning properties of L2/3 neurons. L2/3 neurons were preferentially innervated by dLGN axons contacting L4 neurons that also connected to them. Thus, rather than propagating serially in the canonical dLGN→L4→L2/3 sequence, TC axons simultaneously excite vertically aligned, interdigitated networks of connected pyramidal neurons encompassing L4 and L2/3. As TC axons are present from very early stages of cortical development<sup>43</sup>, vertically aligned

and interconnected sister cells<sup>44</sup> descending from the same cortical precursor could connect preferentially with the same thalamic axons. Multilaminar thalamic innervation could also shape specific columnar networks of connected neurons sharing input from the same TC axons by activity-dependent plasticity mechanisms<sup>45</sup>.

The specificity of the monosynaptic dLGN→L2/3 inputs we found in this study suggests that L2/3 neurons integrate input from L4 as well as a copy of the specific thalamic responses that gave rise to the L4 responses (Fig. 5f). What could be the role of these direct dLGN→L2/3 connections that skip a layer of the processing hierarchy? Similar 'shortcut' connections that specifically connect with related neurons but skip hierarchical levels are useful in artificial neural networks for solving complex nonlinear classification problems. Second-order neurons, by virtue of having access to both the original inputs and the nonlinear transform implemented by first-order neurons, can in turn solve nonlinear classification problems. A canonical example of this computation is the implementation of neural network classifiers of exclusive OR (XOR) inputs<sup>46</sup>. Similarly, having access to related inputs from different processing layers might allow L2/3 neurons to fire with high selectivity for specific stimulus features<sup>47</sup>.

Many local and long-range cortical projections have targets in multiple cortical layers<sup>4,5,23</sup>. Like L2/3 neurons receiving related first- and second-order inputs from dLGN and L4, many other cortical connections could be organized with similar multihierarchical specificity. Future experiments will be needed to determine how prevalent this cortical circuit motif is and the computations it might be implementing.

### METHODS

Methods and any associated references are available in the [online version of the paper](#).

*Note: Any Supplementary Information and Source Data files are available in the online version of the paper.*

### ACKNOWLEDGMENTS

We thank G. Shepherd, S. Peron, B. Atallah, H. Young, M. Fridman, A. Renart, S. Druckmann, T. Marques and C. Machens for comments on the manuscript. This work was supported by fellowships from Fundação para a Ciência e a Tecnologia to N.A.M. and J.B., a Marie Curie (PCIG12-GA-2012-334353) grant and a Human Frontier Science Program grant to L.P. and by the Champalimaud Foundation.

### AUTHOR CONTRIBUTIONS

N.A.M. and L.P. designed the study. L.P. built the experimental setup. N.A.M. performed the experiments. J.B. developed the model. N.A.M. and L.P. analyzed the data. N.A.M. and L.P. wrote the manuscript with input from J.B.

### COMPETING FINANCIAL INTERESTS

The authors declare no competing financial interests.

Reprints and permissions information is available online at <http://www.nature.com/reprints/index.html>.

- Priebe, N.J. & Ferster, D. Mechanisms of neuronal computation in mammalian visual cortex. *Neuron* **75**, 194–208 (2012).
- Reid, R.C. From functional architecture to functional connectomics. *Neuron* **75**, 209–217 (2012).
- Callaway, E.M. Local circuits in primary visual cortex of the macaque monkey. *Annu. Rev. Neurosci.* **21**, 47–74 (1998).
- Douglas, R.J. & Martin, K.A. Neuronal circuits of the neocortex. *Annu. Rev. Neurosci.* **27**, 419–451 (2004).
- Harris, K.D. & Mrsic-Flogel, T.D. Cortical connectivity and sensory coding. *Nature* **503**, 51–58 (2013).
- Sun, W., Tan, Z., Mensh, B.D. & Ji, N. Thalamus provides layer 4 of primary visual cortex with orientation- and direction-tuned inputs. *Nat. Neurosci.* **19**, 308–315 (2016).
- Hubel, D.H. & Wiesel, T.N. Receptive fields, binocular interaction and functional architecture in the cat's visual cortex. *J. Physiol. (Lond.)* **160**, 106–154 (1962).
- Ferster, D., Chung, S. & Wheat, H. Orientation selectivity of thalamic input to simple cells of cat visual cortex. *Nature* **380**, 249–252 (1996).
- Chung, S. & Ferster, D. Strength and orientation tuning of the thalamic input to simple cells revealed by electrically evoked cortical suppression. *Neuron* **20**, 1177–1189 (1998).

10. Lien, A.D. & Scanziani, M. Tuned thalamic excitation is amplified by visual cortical circuits. *Nat. Neurosci.* **16**, 1315–1323 (2013).
11. Li, L.Y., Li, Y.T., Zhou, M., Tao, H.W. & Zhang, L.I. Intracortical multiplication of thalamocortical signals in mouse auditory cortex. *Nat. Neurosci.* **16**, 1179–1181 (2013).
12. Li, Y.T., Ibrahim, L.A., Liu, B.H., Zhang, L.I. & Tao, H.W. Linear transformation of thalamocortical input by intracortical excitation. *Nat. Neurosci.* **16**, 1324–1330 (2013).
13. Douglas, R.J., Koch, C., Mahowald, M., Martin, K.A.C. & Suarez, H.H. Recurrent excitation in neocortical circuits. *Science* **269**, 981–985 (1995).
14. Ben-Yishai, R., Bar-Or, R.L. & Sompolinsky, H. Theory of orientation tuning in visual cortex. *Proc. Natl. Acad. Sci. USA* **92**, 3844–3848 (1995).
15. Somers, D.C., Nelson, S.B. & Sur, M. An emergent model of orientation selectivity in cat visual cortical simple cells. *J. Neurosci.* **15**, 5448–5465 (1995).
16. Song, S., Sjöström, P.J., Reigl, M., Nelson, S. & Chklovskii, D.B. Highly nonrandom features of synaptic connectivity in local cortical circuits. *PLoS Biol.* **3**, e68 (2005).
17. Perin, R., Berger, T.K. & Markram, H. A synaptic organizing principle for cortical neuronal groups. *Proc. Natl. Acad. Sci. USA* **108**, 5419–5424 (2011).
18. Yoshimura, Y., Dantzker, J.L.M. & Callaway, E.M. Excitatory cortical neurons form fine-scale functional networks. *Nature* **433**, 868–873 (2005).
19. Peters, A. & Feldman, M.L. The projection of the lateral geniculate nucleus to area 17 of the rat cerebral cortex. IV. Terminations upon spiny dendrites. *J. Neurocytol.* **6**, 669–689 (1977).
20. Antonini, A., Fagiolini, M. & Stryker, M.P. Anatomical correlates of functional plasticity in mouse visual cortex. *J. Neurosci.* **19**, 4388–4406 (1999).
21. Ji, X.-Y. *et al.* Thalamocortical innervation pattern in mouse auditory and visual cortex: laminar and cell-type specificity. *Cereb. Cortex* **26**, 2612–2625 (2016).
22. Petreanu, L., Huber, D., Sobczyk, A. & Svoboda, K. Channelrhodopsin-2-assisted circuit mapping of long-range callosal projections. *Nat. Neurosci.* **10**, 663–668 (2007).
23. Petreanu, L., Mao, T., Sternson, S.M. & Svoboda, K. The subcellular organization of neocortical excitatory connections. *Nature* **457**, 1142–1145 (2009).
24. Cruikshank, S.J., Urabe, H., Nurmikko, A.V. & Connors, B.W. Pathway-specific feedforward circuits between thalamus and neocortex revealed by selective optical stimulation of axons. *Neuron* **65**, 230–245 (2010).
25. Cruikshank, S.J., Lewis, T.J. & Connors, B.W. Synaptic basis for intense thalamocortical activation of feedforward inhibitory cells in neocortex. *Nat. Neurosci.* **10**, 462–468 (2007).
26. Gabernet, L., Jadhav, S.P., Feldman, D.E., Carandini, M. & Scanziani, M. Somatosensory integration controlled by dynamic thalamocortical feed-forward inhibition. *Neuron* **48**, 315–327 (2005).
27. Inoue, T. & Imoto, K. Feedforward inhibitory connections from multiple thalamic cells to multiple regular-spiking cells in layer 4 of the somatosensory cortex. *J. Neurophysiol.* **96**, 1746–1754 (2006).
28. Blitz, D.M. & Regehr, W.G. Timing and specificity of feed-forward inhibition within the LGN. *Neuron* **45**, 917–928 (2005).
29. Kampa, B.M., Letzkus, J.J. & Stuart, G.J. Cortical feed-forward networks for binding different streams of sensory information. *Nat. Neurosci.* **9**, 1472–1473 (2006).
30. Yoshimura, Y. & Callaway, E.M. Fine-scale specificity of cortical networks depends on inhibitory cell type and connectivity. *Nat. Neurosci.* **8**, 1552–1559 (2005).
31. Stratford, K.J., Tarczy-Hornoch, K., Martin, K.A.C., Bannister, N.J. & Jack, J.J.B. Excitatory synaptic inputs to spiny stellate cells in cat visual cortex. *Nature* **382**, 258–261 (1996).
32. Gil, Z., Connors, B.W. & Amitai, Y. Efficacy of thalamocortical and intracortical synaptic connections: quanta, innervation, and reliability. *Neuron* **23**, 385–397 (1999).
33. Kloc, M. & Maffei, A. Target-specific properties of thalamocortical synapses onto layer 4 of mouse primary visual cortex. *J. Neurosci.* **34**, 15455–15465 (2014).
34. Jin, J., Wang, Y., Swadlow, H.A. & Alonso, J.M. Population receptive fields of ON and OFF thalamic inputs to an orientation column in visual cortex. *Nat. Neurosci.* **14**, 232–238 (2011).
35. Reid, R.C. & Alonso, J.M. Specificity of monosynaptic connections from thalamus to visual cortex. *Nature* **378**, 281–284 (1995).
36. Ko, H. *et al.* Functional specificity of local synaptic connections in neocortical networks. *Nature* **473**, 87–91 (2011).
37. Cossell, L. *et al.* Functional organization of excitatory synaptic strength in primary visual cortex. *Nature* **518**, 399–403 (2015).
38. Wertz, A. *et al.* Presynaptic networks. Single-cell-initiated monosynaptic tracing reveals layer-specific cortical network modules. *Science* **349**, 70–74 (2015).
39. Constantinople, C.M. & Bruno, R.M. Deep cortical layers are activated directly by thalamus. *Science* **340**, 1591–1594 (2013).
40. Lefort, S., Tómm, C., Floyd Sarria, J.-C. & Petersen, C.C.H. The excitatory neuronal network of the C2 barrel column in mouse primary somatosensory cortex. *Neuron* **61**, 301–316 (2009).
41. Binzegger, T., Douglas, R.J. & Martin, K.A.C. A quantitative map of the circuit of cat primary visual cortex. *J. Neurosci.* **24**, 8441–8453 (2004).
42. Shepherd, G.M.G., Polgruto, T.A. & Svoboda, K. Circuit analysis of experience-dependent plasticity in the developing rat barrel cortex. *Neuron* **38**, 277–289 (2003).
43. López-Bendito, G. & Molnár, Z. Thalamocortical development: how are we going to get there? *Nat. Rev. Neurosci.* **4**, 276–289 (2003).
44. Yu, Y.-C., Bultje, R.S., Wang, X. & Shi, S.-H. Specific synapses develop preferentially among sister excitatory neurons in the neocortex. *Nature* **458**, 501–504 (2009).
45. Ko, H. *et al.* The emergence of functional microcircuits in visual cortex. *Nature* **496**, 96–100 (2013).
46. Hertz, J., Krogh, A. & Palmer, R. *Introduction to the Theory of Neural Computation* (Addison Wesley, 1991).
47. Petersen, C.C.H. & Crochet, S. Synaptic computation and sensory processing in neocortical layer 2/3. *Neuron* **78**, 28–48 (2013).

## ONLINE METHODS

**Animal surgeries.** All procedures were reviewed by the Champalimaud Centre for the Unknown Ethics Committee and performed in accordance of the Portuguese Veterinary General Direction guidelines. Surgeries were conducted in either male or female C57BL/6J mice (P13–P15) under isoflurane anesthesia (2%). Virus expressing ChR2 (AAV-2/1-CAG-Channelrhodopsin-2-Venus<sup>23</sup>, University of Pennsylvania Gene Therapy Program Vector Core) were delivered to dLGN (20 nl, 10 nl min<sup>-1</sup>, coordinates relative to bregma: 1.6 mm posterior, 2.1 mm lateral, 2.64 mm deep) using beveled pulled glass pipettes (Drummond Scientific) of ~20-μm tip size. Animals were maintained at 37 °C and fully recovered on a heating pad before returning to their home cages, where they stayed with their mother until weaning date (P21) or euthanasia. Mice older than P21 were housed in same-sex groups of up to 5 animals per cage. All animals were housed in a room with a regular 12 h light/dark cycle.

**Slice preparation.** Four to 12 days (age range: P18 – P25) after the viral infections, mice were intracardially perfused with ice-cold artificial cerebrospinal fluid (aCSF, 127 mM NaCl, 25 mM NaHCO<sub>3</sub>, 25 mM D-glucose, 2.5 mM KCl, 1 mM MgCl<sub>2</sub>, 2 mM CaCl<sub>2</sub> and 1.25 mM NaH<sub>2</sub>PO<sub>4</sub>, aerated with 95% O<sub>2</sub>/5% CO<sub>2</sub>) and decapitated under deep anesthesia (intraperitoneal, 75 mg/kg ketamine, 1 mg/kg medetomidine). Brains were dissected in ice-chilled choline chloride solution (110 mM choline chloride, 25 mM NaHCO<sub>3</sub>, 25 mM D-glucose, 11.6 mM sodium ascorbate, 7 mM MgCl<sub>2</sub>, 3.1 mM sodium pyruvate, 2.5 mM KCl, 1.25 mM NaH<sub>2</sub>PO<sub>4</sub> and 0.5 mM CaCl<sub>2</sub>, aerated with 95% O<sub>2</sub>/5% CO<sub>2</sub>) and sliced in 300-μm-thick coronal slices using a Leica VT1200S vibratome. Slices were then incubated for 30 min at 37 °C in aCSF. dLGN infection was confirmed under a 4× magnification objective using a fluorescence filter for Venus visualization.

**Electrophysiology and photostimulation.** Data were recorded using Multiclamp 700A and Multiclamp 700B amplifiers (Axon Instruments), digitalized using National Instruments acquisition boards controlled under Matlab using Ephus (ref. 48). Neurons were patched with borosilicate pipettes (resistance 3–5 MΩ, Werner Instruments) filled with potassium gluconate internal solution (128 mM potassium gluconate, 4 mM MgCl<sub>2</sub>, 10 mM HEPES, 1 mM EGTA, 4 mM Na<sub>2</sub>ATP, 0.4 mM Na<sub>2</sub>GTP, 10 mM sodium phosphocreatine, 3 mM sodium L-ascorbate, 3 mg/mL biocytin (Sigma) and 5 μg/mL Alexa-594 (Molecular Probes); pH 7.25, 290 mOsm). All recordings were performed at room temperature (22–24 °C) and in the presence of 3-((R)-2-carboxypiperazin-4-yl)-propyl-1-phosphonic acid (CPP, 5 μM) in the bath. Recorded cells were >40 μm under the slice surface. The mean intersomatic distance of simultaneously recorded L4 pairs was 42.86 ± 16.35 μm, 62.81 ± 27.18 μm for L2/3 pairs and that of translaminar pairs was 195.44 ± 35.24 μm for L4→L2/3 (Supplementary Fig. 7). A low noise (<1% rms) blue laser (473 nm, CNI Laser) was used for photostimulation. Duration and intensities of light pulses were controlled with a Pockels cell (ConOptics) and a shutter (Thorlabs). As expression level of ChR2 varies across animals, laser power at the sample was manually adjusted in each experiment using a graduated neutral density filter (EdmundOptics) so that responses of ~100 pA were evoked in the most excitable locations (mean 291.1 ± 391 μW, range 0.3–1,467 μW). The laser beam was rapidly repositioned using galvanometer mirrors (Thorlabs) using Ephus. For correlation experiments multiple neurons (2–3) were simultaneously recorded in voltage-clamp (–70 mV). We delivered 2-ms light pulses in an 8 × 8 grid pattern with 60-μm spacing spanning 420 μm<sup>2</sup>. The grid covered most of L4 and L2/3 (Fig. 2b and Supplementary Fig. 3j,n) or was centered on L4 for experiments involving only L4 pairs (Supplementary Fig. 3b,f). A different location on the grid was illuminated every 750 ms with 4 light pulses at 10 Hz in a pseudorandom sequence to maximize time between neighboring locations<sup>42</sup>. Only responses to the first photostimulation pulse were used in all analyses. Input resistance was constantly monitored by delivering a test voltage pulse at the end of each photostimulation. Individual locations were repeatedly stimulated every ~50 s at least 15 times (mean 24.76 ± 5.85 times). There was no relation between the number of photostimulations and the number of correlated locations. For most pairs we also repeated the grid of photostimulation in current-clamp mode to verify that L4 and L2/3 never reached spiking threshold (Supplementary Fig. 4). Local connectivity across recorded pairs was repeatedly assessed (100 times) in current-clamp mode using depolarizing current steps (400–600 pA, 10 ms, interstimulus interval 300 ms) to evoke action potentials in one neuron while monitoring the activity in the other and vice versa. In general

the investigator was blind to the local connectivity of the recorded pairs during the experiments. For some L4→L2/3 recordings, connectivity analyses were done before photostimulation in order to balance data groups and increase data collection from the relatively rare L4→L2/3 connected pairs. A set of square current steps were used in current clamp mode to measure input/output curves and to confirm that the recorded neurons were pyramidal by their characteristic spiking pattern (Fig. 4a,d). The pyramidal morphology of the recorded neurons was also confirmed with fluorescence imaging of the recorded neuron using a CCD camera (Qimaging Retiga 2000) and by *post hoc* reconstructions of their dendrites. Neurons with resting potentials higher than –50 mV at break-in were discarded. sCRACM experiments were performed by photostimulating dLGN axons in a 12 by 24 grid pattern with 50-μm spacing over the dendrites of the recorded neurons in the presence of TTX (1 μM) and 4-AP (100 μM) in the bath as previously described<sup>23</sup>. The sCRACM method has a resolution of ~50 μm, ChR2<sup>+</sup> synapses being photostimulated up to 60 μm away from their location in the dendritic tree<sup>23</sup>. sCRACM maps from neurons with detectable input (total sCRACM input > 5 times the total input during baseline period) were normalized and averaged in Figure 1c,d and Supplementary Figure 1. Maps were linearly interpolated for display only in Figure 1c,d and Supplementary Figure 1.

**Immunohistochemistry and neuronal reconstruction.** After patching, biocytin-filled neurons were fixed overnight in 4% paraformaldehyde. Slices were rinsed in phosphate buffer (PB) 0.1 M. Endogenous peroxidases were quenched with 1% H<sub>2</sub>O<sub>2</sub> (Sigma) in PB 0.1 M for 30 min at room temperature. Slices were rinsed again in PB 0.1 M and then incubated in the ABC reaction (Vector Laboratories) for 6–8 h at room temperature (22–24 °C). After successive PB 0.1 M and Tris buffered saline (TBS) washings, slices were subjected to the diaminobenzidine (DAB) reaction for 5–20 min (prepared fresh each time using 30 mL of TBS, 90 μL 3% H<sub>2</sub>O<sub>2</sub>, 225 μL of NiCl<sub>2</sub> (250 mM) and 7 mg of DAB (Sigma)). The DAB reaction was stopped with TBS. Slices were then mounted and coverslipped with Mowiol (Sigma) mounting media. Dendrites were reconstructed under a 40× magnification objective using an Olympus BX61 microscope and Neurolucida software (MBF Bioscience). Tracings were imported into Matlab, corrected for shrinkage and analyzed using custom routines. Dendritic length density (Fig. 1d) was calculated in 50-μm bins.

**Confocal images.** AAV-2/1-CAG-ChR2-Venus-injected animals were intracardially perfused with 4% paraformaldehyde (7 d after surgery) and sectioned in 75-μm thick coronal slices. Slices were stained for DAPI and then imaged using a confocal microscope (Zeiss LSM 710). The visual cortex of 3 mice was imaged using a 40× objective. Vertical fluorescence profiles of Venus expressing axons in V1 were measured using ImageJ.

**Definition of cortical layers.** The boundaries between layers were established as L1: pia–100 μm; L2/3: 100–350 μm; L4: 350–500 μm; L5: 500–750 μm; L6: 750–950 μm. To correct for variations in cortical thickness due to differences in slicing angles, the laminar position of each recorded neuron was calculated as a fraction of the total cortical thickness for each experiment. All the recorded neurons were then positioned on a reference cortical slice with an average thickness.

**Data analysis.** To classify pairs of neurons as connected or nonconnected, we scored local connections by detecting suprathreshold responses in postsynaptic neurons (3-fold over the s.d. of the baseline period) in a window (5 to 20 ms) after the depolarization pulse. Mean synaptic response (Table 1) was calculated as the difference between baseline and the mean depolarization in a 1-ms window centered on the highest peak in the detection window and then averaged across repetitions. Coefficient of variation (Table 1) was calculated as

$$(\sigma_s^2 - \sigma_n^2)^{1/2} / \mu_s$$

where  $\sigma_s$  is the variance of the synaptic responses and  $\sigma_n$  is the variance of the noise. Noise was calculated the same way that the mean synaptic responses in 4 different baseline time points.  $\mu_s$  is the mean synaptic response. In photostimulation experiments, eEPSCs were scored as responses if a threshold of 4 times the s.d. of the baseline period (100 ms before photostimulation) was crossed 2 to 18 ms after photostimulation. Response probability was then calculated by dividing the number of responses over the total number of photostimulation



repetitions. eEPSC charge was calculated in a 60-ms window starting with each photostimulation.

Unitary TC inputs to L4 and L2/3 were calculated by averaging eEPSC charges in successful trials from photostimulated locations with a response probability between 0.35 and 0.8 in the recorded neuron.

eEPSC confluations across photostimulation trials in simultaneously recorded neurons were quantified by calculating the Pearson's correlation coefficient of their amplitudes (peak response in a 40-ms window). The confidence interval around the measured correlation coefficient was measured by bootstrapping 10,000 times ( $\alpha = 0.001$ , bootci function in Matlab). Locations where the lower boundary of the confidence interval was greater than zero were considered correlated (Figs. 2, 4 and 5).

To test the effect of local connectivity on correlations (Figs. 4 and 5), the mean eEPSCs for the pair from each location were sorted according to their charge in units of mean number of inputs (mean charge for the pair/unitary TC charge) and binned (bin size 1). When analyzing L4→L2/3 pairs (Fig. 5), the mean of the unitary TC inputs to L4 and L2/3 was used to estimate the number of inputs. While the mean number of inputs is not an accurate estimation of the number of stimulated axons, as shared axons count twice, it is an experimentally measurable quantity to which correlations are related (Fig. 3e). The fraction of correlated locations increases as a function of the mean number of inputs and shared input is only comparable between locations with a similar range of number of inputs (Fig. 3). For group comparisons in Figures 4c,f and 5e, we compared for each pair locations recruiting between 0.4 and 2.5 mean number of inputs as this range contained most of the responses (Supplementary Figs. 3 and 5). No data points were excluded. Full data are shown in Supplementary Figure 5.

To estimate the relative laminar density of connected axons to L4 and L2/3 (Fig. 5c), we averaged 5 photostimulation experiments for each cell of vertically aligned pairs. eEPSC responses at each location were averaged 0–75 ms after the photostimulation pulse. Average maps were aligned to the pia location and normalized to their largest response. Group averages were normalized to estimate the relative density distribution of axons contacting either L4 or L2/3 pyramidal neurons. Laminar profiles were calculated by averaging responses across columns for each individual map and then averaging across experiments. Group averages were linearly interpolated for display in Figure 5c.

**Statistical analyses.** No statistical tests were used to predetermine sample sizes, but our sample sizes are similar to those in previous studies<sup>18,30</sup>. All statistical analyses were performed with Matlab. Data distribution was assumed to be normal for large sample sizes, but this was not formally tested. When normality of the data was uncertain, we used nonparametric tests as described in the text and figure legends. Two-tailed comparison tests were used. Data in the text are presented as mean  $\pm$  s.d. unless otherwise indicated.

A **Supplementary Methods Checklist** is available.

**Model and simulations.** We defined three ensembles of axons contacting two neurons ( $E_1$ ,  $E_2$  and  $E_3$ ). The membrane potentials of the two neurons ( $\omega_1$ ,  $\omega_2$ ) are expressed in numbers of unitary inputs. Axons from  $E_1$  and  $E_3$  only contribute to  $\omega_1$  and  $\omega_2$ , respectively, while axons from  $E_2$  contribute to both  $\omega_1$  and  $\omega_2$  (Fig. 3a). Independent spiking events for each axon  $i$  upon photostimulation are defined as binary variables  $e_i \in \{0, 1\}$ ,  $i = 1, 2, \dots, N$ , with probability  $p_i$ , where  $N$  is the total number axons for a given location. As a binary probabilistic process, spiking events follow a Bernoulli distribution with variance  $p_i(1 - p_i)$ . Measurement of  $\omega_1$  and  $\omega_2$  is affected by uncorrelated noise. This noise is a random variable  $\xi$  of zero mean and variance  $\gamma$  that is independent of laser power. Thus, on a given photostimulation trial the inputs to the two neurons are

$$\begin{cases} \omega_1 = x_1 + x_2 + \xi_1 \\ \omega_2 = x_2 + x_3 + \xi_2 \end{cases}$$

where independent random variables  $x_1$ ,  $x_2$  and  $x_3$  are the summed numbers of activated axons from each ensemble ( $\Sigma e_i$ ). Across locations, there are on average

$N_2 = N \times r$  shared axons (Fig. 3a), where  $r$  is the proportion of axons shared by  $\omega_1$  and  $\omega_2$ . The spiking events of the shared axons ( $E_2$ ) contribute to the joint activity of the two neurons (Fig. 3b, bottom panel):

$$\text{cov}(\omega_1, \omega_2) = \text{var}(x_2) \quad (1)$$

The variance of  $x_2$  is expressed as

$$\text{var}(x_2) = \sum_{i \in E_2} p_i(1 - p_i)$$

where the spike probability of each axon,  $p_i$ , is modulated by the power of stimulation,  $P$ , as  $p_i = g(P - \theta_i)$ . Based on previous experimental measurements<sup>22</sup>, we modeled  $g$  as a cumulative Gaussian distribution function of zero mean and s.d.  $\sigma_s$  (Fig. 3b, top panel).  $\theta_i$  is the threshold for each axon  $i$ . Thus,

$$\text{var}(x_2) = \sum_{i \in E_2} g(P - \theta_i)(1 - g(P - \theta_i))$$

Given equation (1), the correlations can be expressed as

$$\text{corr}(\omega_1, \omega_2) = \frac{\text{var}(x_2)}{\sqrt{\text{var}(x_1) + \text{var}(x_2) + \gamma} \sqrt{\text{var}(x_3) + \text{var}(x_2) + \gamma}}$$

Correlations are well defined even when  $P = 0$  because  $\gamma$  is strictly a positive real number. When the power is too low or too high the mean correlation falls to zero.

Experimentally, at any given photostimulation location, the number of axons on each ensemble ( $N_1$ ,  $N_2$ ,  $N_3$ ) and the axonal thresholds  $\{\theta_i\}$  are different. For the plot in Figure 3d,e, we simulated sampling axons from different locations with fixed laser power. Axons were randomly assigned to the  $E_1$ ,  $E_2$  or  $E_3$  connectivity groups with probabilities

$$\frac{1-r}{2}, r, \frac{1-r}{2}$$

respectively. In Figure 3d the total number of axons ( $N$ ) varied from 2 to 30. In Figure 3e the number of axons was fixed at 40. Each axon had a threshold  $\theta$  sampled from a Gaussian probability distribution with mean 20 (a.u. of power) and s.d. 5 (a.u. of power). Laser power was fixed at 10 a.u. in all simulations. The variance of the noise,  $\gamma$ , was 0.2 squared unitary inputs. The sigmoid  $g$  was a cumulative Gaussian distribution centered at zero and with an s.d. of 2. The tested fractions of shared axons  $r$  were 0.1, 0.2, 0.3 and 0.4. We obtained values of Pearson's correlation coefficient  $\text{corr}(\omega_1, \omega_2)$  after 20 trials. By bootstrapping 10,000 times we estimated 99.5% confidence intervals around the value of  $\text{corr}(\omega_1, \omega_2)$ . We considered the simulated locations correlated when the lower boundaries of the confidence intervals were greater than zero. Figure 3d shows the fractions of correlated locations after simulating each value of number of axons 5,000 times. Figure 3e was obtained after 20,000 simulations and plotting the fraction of correlated locations as a function of the mean number of evoked inputs on the pair. The number of evoked inputs per trial  $I$  corresponds to the number of spiking axons, where shared axons count double:

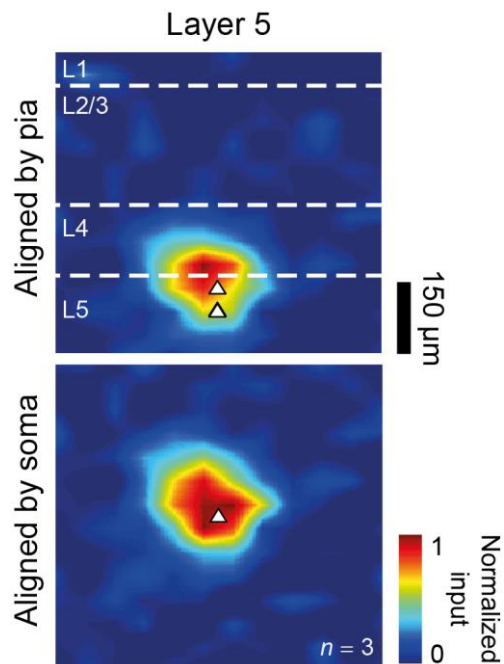
$$I = \sum_{i \in E_1} e_i + 2 \sum_{i \in E_2} e_i + \sum_{i \in E_3} e_i$$

The mean of  $I$  across trials, the mean number of inputs, is measured for recorded pairs and plotted in Figures 2d, 4b,e and 5d. Data were grouped in bins of 0.1.

**Code availability.** No special code was used for this study.

**Data availability.** The data that support the findings of this study are available from the corresponding author upon request.

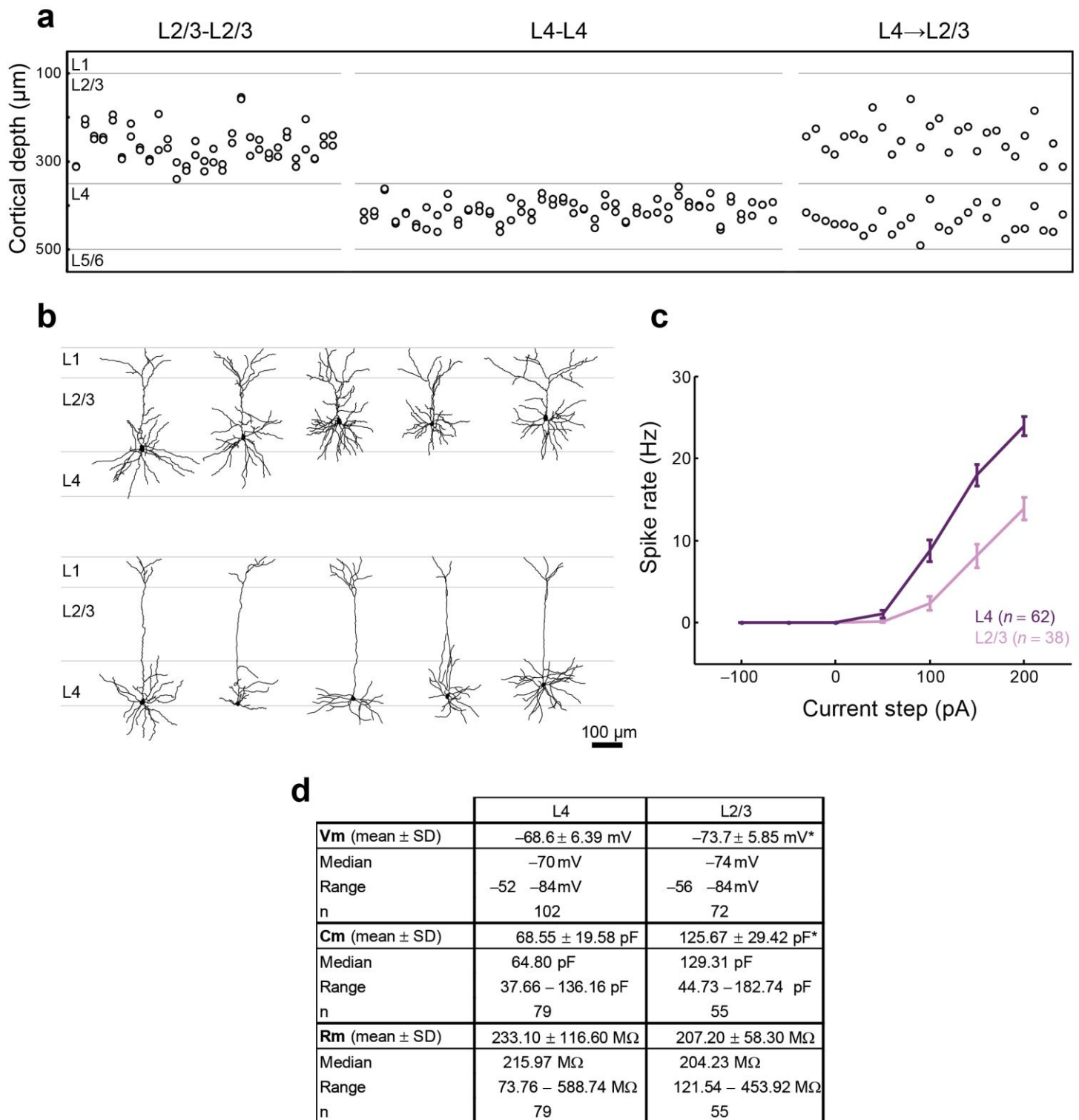
48. Suter, B.A. *et al.* Ephus: multipurpose data acquisition software for neuroscience experiments. *Front. Neural Circuits* 4, 100 (2010).



Supplementary Figure 1

dLGN inputs innervate L5 pyramidal neurons in V1.

Top. Average sCRACM maps aligned by pia position (white triangles, soma position). Bottom. Average sCRACM maps aligned by soma. Only neurons receiving significant dLGN inputs (3 out of 11 neurons) are plotted.

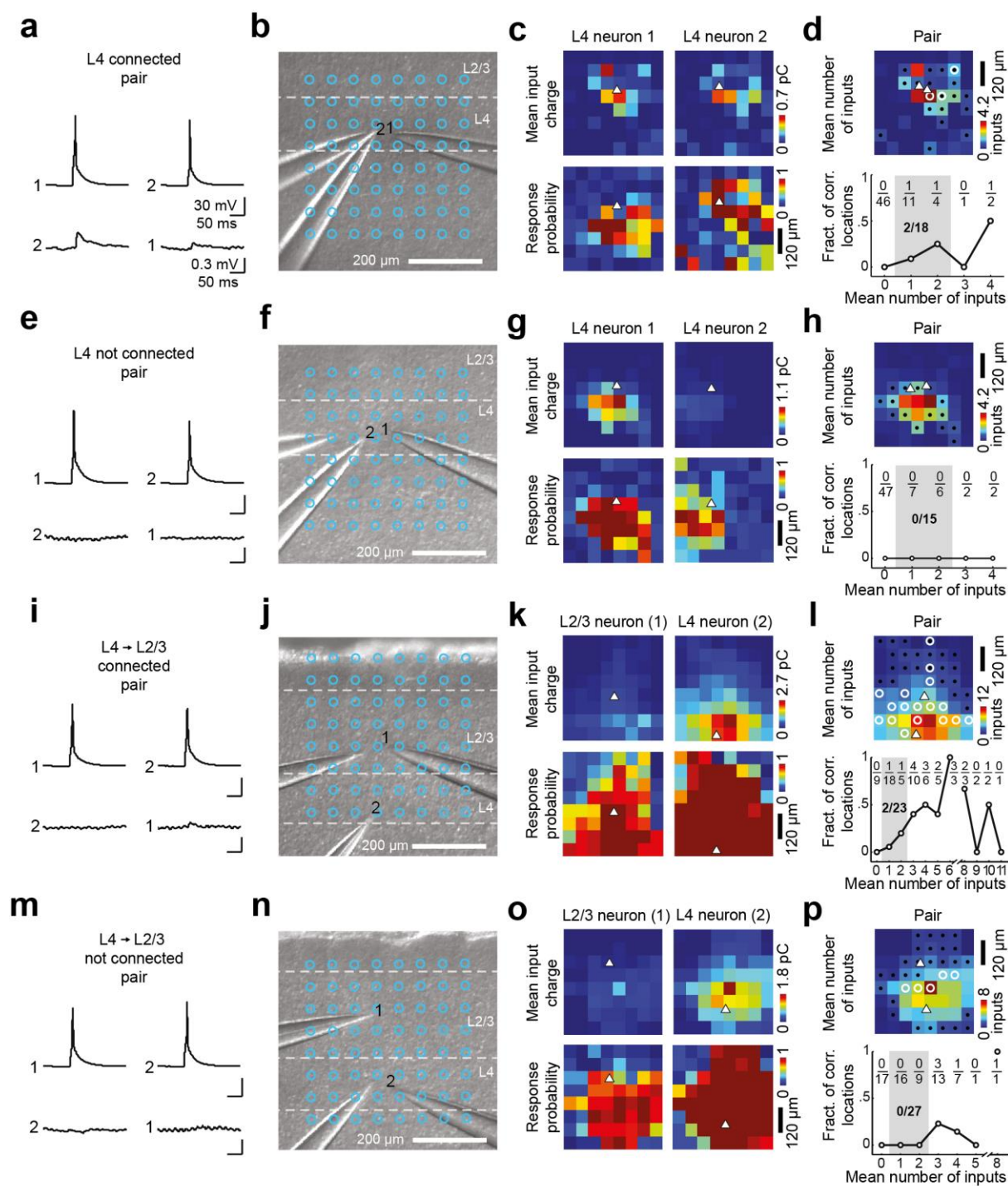


**Supplementary Figure 2**

Laminar, morphological and electrophysiological differences between L4 and L2/3 pyramidal neurons. **(a)** Laminar position of paired recorded neurons in L4, L2/3 or L4 and L2/3. **(b)** Neuronal dendritic morphology reconstructions from L2/3 (top) or L4 (bottom) neurons. **(c)** Input/output curves from L2/3

or L4 neurons. **(d)** Intrinsic properties of L4 and L2/3 recorded neurons. Vm:  $P = 3.02 \times 10^{-7}$ , t-test ( $t_{172} = -5.33$ ). Cm:  $P = 1.24 \times 10^{-26}$ , t-test ( $t_{132} = -13.5$ ). Rm:  $P = 0.1312$ , t-test ( $t_{132} = 1.52$ ). Vm: membrane resting potential. Cm: membrane capacitance. Rm: membrane resistance.





### Supplementary Figure 3

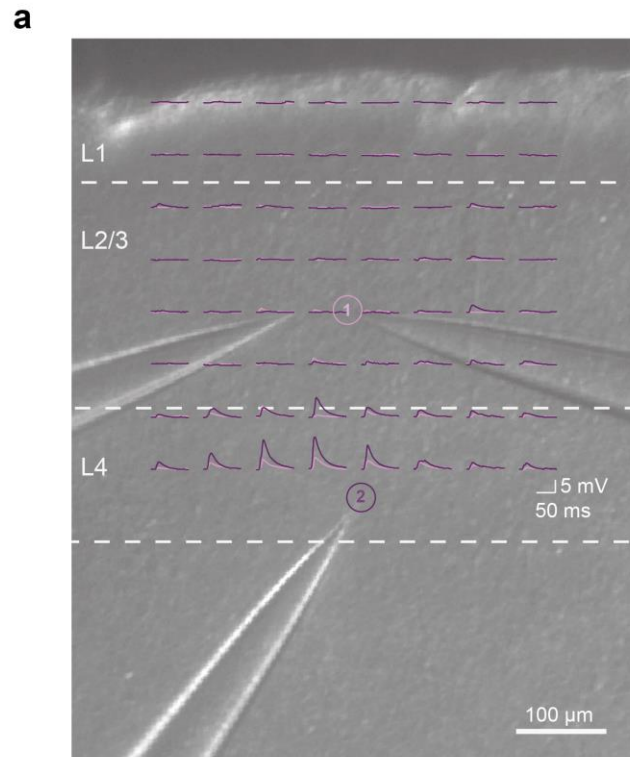
Example experiments from connected and nonconnected pairs of neurons in V1.

**(a,e,i,m)** Local connectivity test. Presynaptic spiking elicited for each neuron (top) and the traces simultaneously recorded in the other neuron (bottom). Traces are the mean of 100 repetitions.

**(b,f,j,n)** Brightfield image of the brain slice showing the recording pipettes and the photostimulation grid.

**(c,g,k,o)** Maps of mean eEPSC charge (top) and response probability (bottom) across photostimulated locations in **b,f,j,n** respectively for each neuron in the pair. White triangles, soma position.

**(d,h,l,p)** Top, map of mean number of inputs recruited for the pair at each photostimulated location in the grid (average of top panels in **c,g,k,o** respectively). Mean number of inputs is calculated as the mean eEPSC charge for the pair / TC unitary input size. White circles indicate locations with correlated eEPSCs. Bottom, fraction of correlated locations as function of mean number of inputs. Bin size, 1 input. Shaded area, range used for analyses in **Fig. 4** and **Fig. 5**. Pixels with values within that range are marked with black dots in top panel.



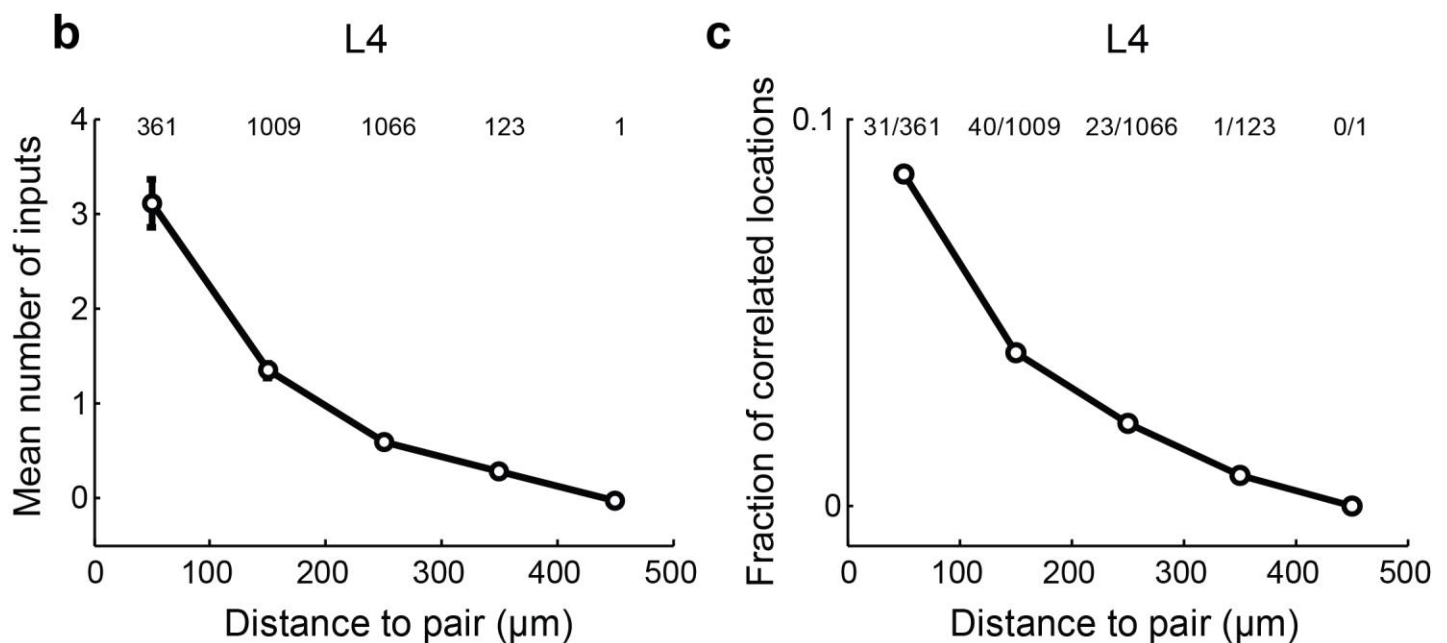
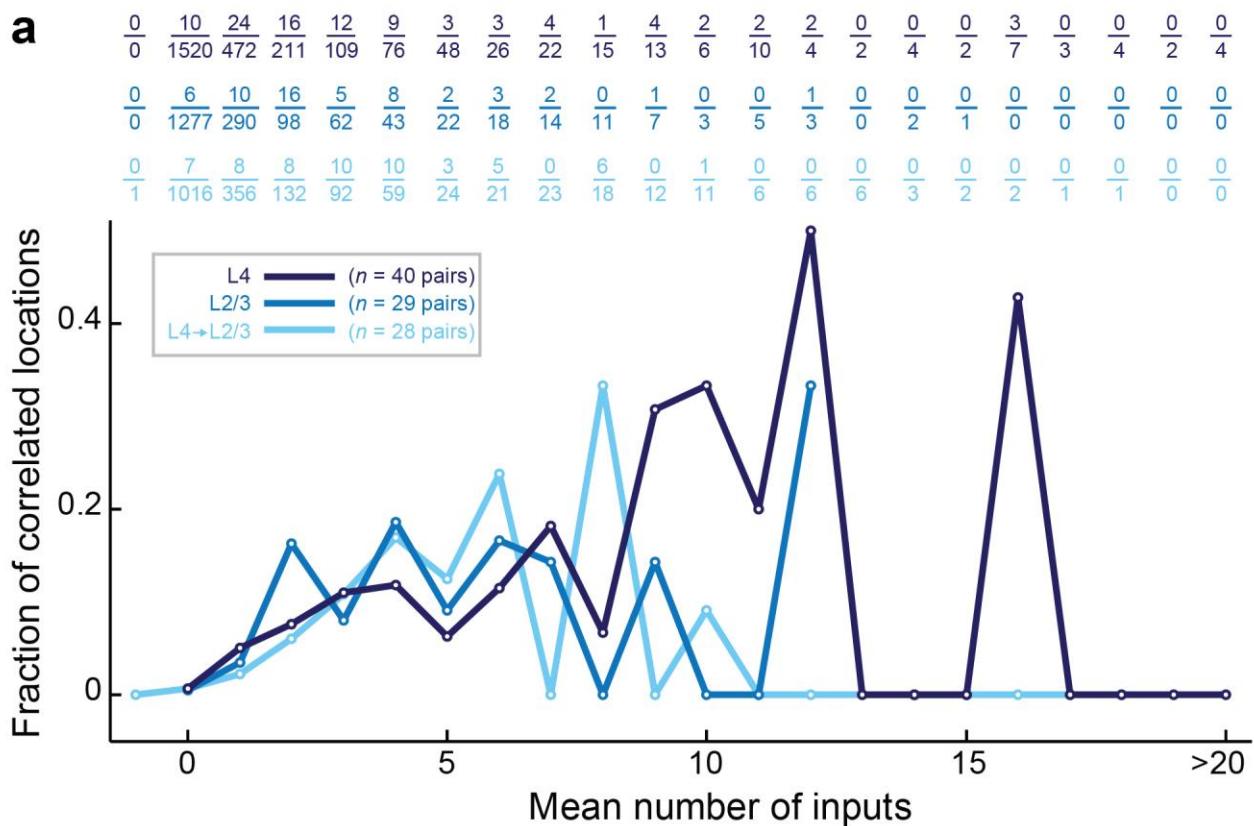
**b**

	L4	L2/3
Neurons	72	65
Number of stimulations	4608	4160
Maximum eEPSP (mean $\pm$ SD)	7.22 $\pm$ 4.53 mV	3.98 $\pm$ 2.97 mV
Spike number	0	0
Spike probability	0	0

**Supplementary Figure 4**

Photostimulation fails to evoke suprathreshold responses in V1 neurons.

(a) Example photostimulation experiment in current-clamp showing subthreshold membrane potential depolarizations evoked at each location for a pair of neurons (circles). (b) Summary table for depolarizations recorded in current-clamp from L2/3 and L4 neurons.



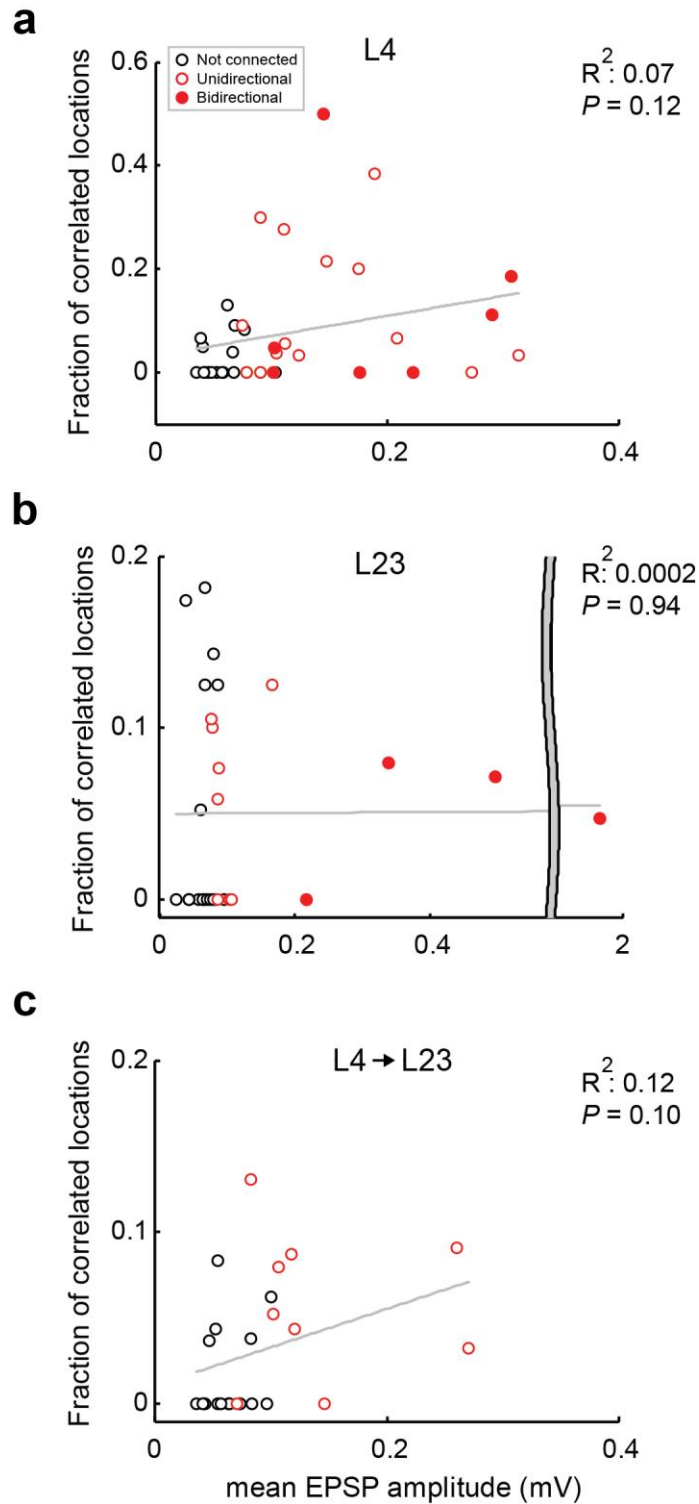
**Supplementary Figure 5**

The fraction of correlated locations increases with the number of recruited inputs.

(a) Fraction of locations with correlated inputs as a function of the mean number of inputs recruited from all photostimulated locations and all the pairs in L4, L2/3 or L4→L2/3 (connected and not connected pairs pooled together). Bin size 1 input. Exact fraction of correlated locations in each bin



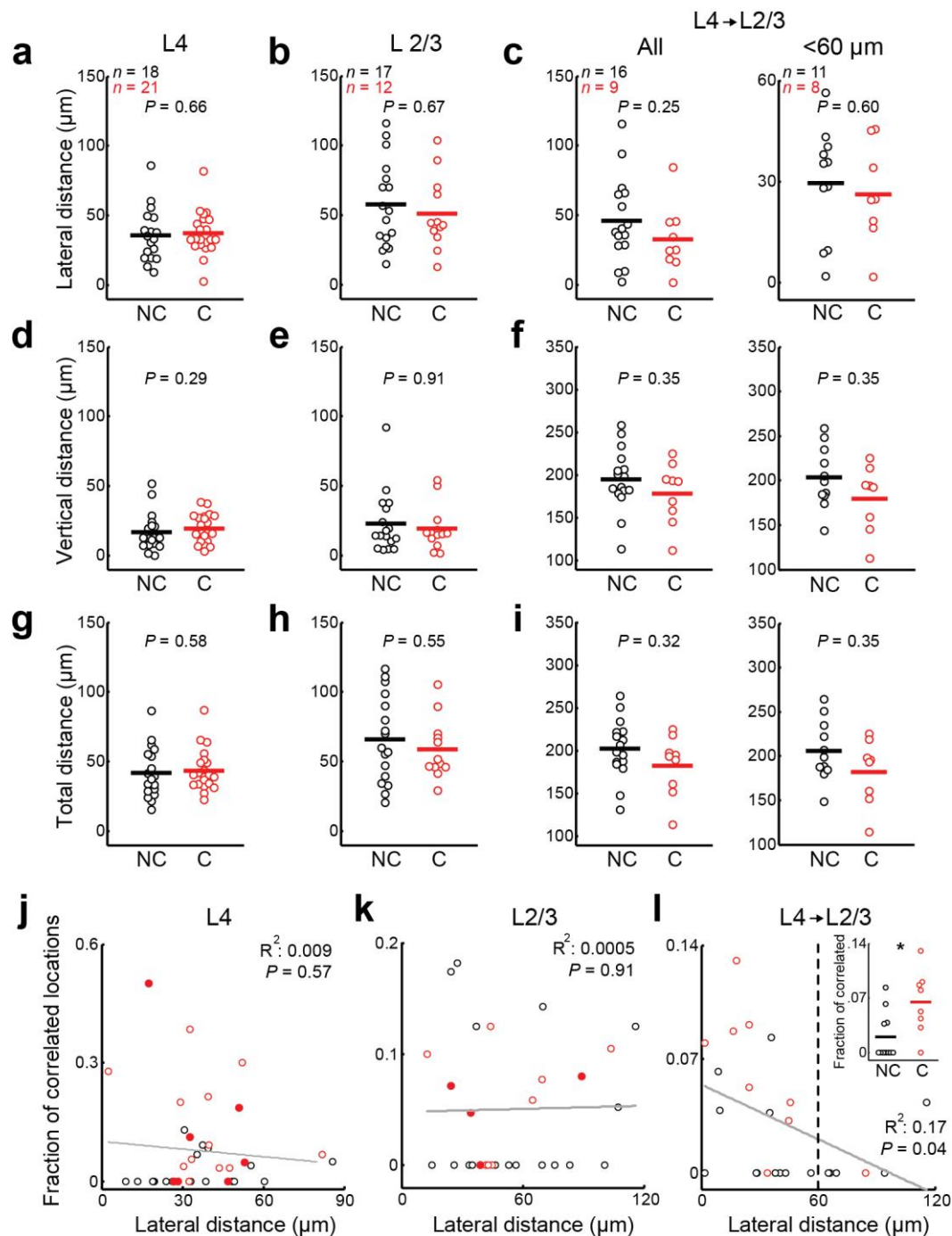
are shown for L4, L2/3 and L4→L2/3 pairs. First 4 bins are the same data as in **Fig. 4 b, e** and **Fig. 5 d**. **(b)** Mean number of inputs versus distance of the photostimulated locations to each L4 pair (center of both somata). Bin size, 100  $\mu\text{m}$ . The number of locations in each bin is shown. **(c)** Fraction of correlated locations as function of distance to the pair for all L4 pairs. Bin size, 100  $\mu\text{m}$ . The fraction of correlated locations in each bin is shown. The number of inputs recruited is larger in perisomatic areas resulting in a larger fraction of correlated locations close to the somata in L4 pairs.



**Supplementary Figure 6**

Connection strength is a weak predictor of shared input.

Relationship between the fraction of correlated locations and the connection strength for L4 (**a**), L2/3 (**b**) and L4→L2/3 (**c**) pairs. Gray line, linear regression fit.



**Supplementary Figure 7**

Intersomatic distances of the recorded pairs.

Lateral (**a,b,c**), vertical (**d,e,f**) and total distance (**g,h,i**) for the connected and not connected pairs in each group. L4→L2/3 distances are shown for all pairs (left) or only the pairs within 60  $\mu\text{m}$  of lateral distance (right).  $P$  value for Wilcoxon rank sum test between groups is shown in each panel.

Horizontal lines, mean. (**j,k,l**) Fraction of correlated locations as function of lateral distance for L4, L2/3 and L4→L2/3 pairs. Gray line, linear regression fit. Filled dots, bidirectionally connected pairs. For L4→L2/3 pairs there was a significant effect of horizontal distance on the fraction of correlated

locations. However, as there was only one connected pair at distances  $> 60\ \mu\text{m}$ , the effect could be due to connectivity and not distance. To disambiguate this we compared correlations only for pairs  $< 60\ \mu\text{m}$  apart. While lateral displacement was very similar across the two groups (panel **c**, right), the fraction of correlated locations was still larger in the connected group (inset in panel **I**, fraction of correlated locations for individual vertical pairs within  $60\ \mu\text{m}$  of lateral distance;  $P < 0.02$  Wilcoxon rank sum test).